Journal of Environmental Chemical Engineering 12 (2024) 112752

Contents lists available at ScienceDirect

Journal of Environmental Chemical Engineering

journal homepage: www.elsevier.com/locate/jece

Wavelength-dependent activity screening of reduced titania for photocatalytic degradation of imidacloprid in batch and flow-mode

Anca Roibu [a,*], Razvan Udroiu [b], Coset Abreu-Jaureguí [c], Joaquin Silvestre-Albero [c], Luminita Andronic [a,*]

[a] Product Design, Mechatronics and Environment Department, Transilvania University of Brasov, Romania
[b] Manufacturing Engineering Department, Transilvania University of Brasov, Romania
[c] Laboratorio de Materiales Avanzados, Departamento de Química Inorgánica – Instituto Universitario de Materiales, Universidad de Alicante, Spain

ARTICLE INFO

Keywords:
Reduced titania
Visible-light
Water treatment
Screening
3-D printing
Microreactor

ABSTRACT

Water reuse is an emerging solution to decrease pressure on freshwater supplies and meet the increasing demand. This study explores the use of semiconductor photocatalysis for pesticide removal, focusing on extending TiO_2 absorption to visible light and accelerating the screening of its wavelength-dependent photocatalytic activity. Grey to black TiO_2 photocatalysts with lower direct and indirect band gap energies, up to 1.56 eV and 2.16 eV, respectively, were prepared by the chemical reduction of titania P25. The XPS analysis showed considerable oxygen vacancies, especially at the highest reduction temperature of 400 °C. The fraction of oxygen in the TiO_2 lattice decreased from 90 % in the case of P25 to 53% for the photocatalyst obtained at 400 °C. The wavelength-dependent photocatalytic activity for the degradation of imidacloprid was screened in a batch photoreactor. TiO_2 P25 presented higher photocatalytic activity than the reduced materials at 400 and 413 nm. At 443 nm, the material reduced at 400 °C exhibited the highest degradation efficiency of 16.8 % compared to 4.2 % as found for P25. Selected photocatalysts were then immobilized as thin films and tested in a 3D-printed flow photoreactor. Wavelength and photocatalyst's impact on imidacloprid degradation in flow mode aligned with batch mode observations. The film activity remained stable after multiple reaction conditions and at least 150 min of operation. The proposed in-flow screening strategy is a promising approach to rapidly identify visible-light active catalysts, while minimizing the consumption of photocatalytic material and water contaminated with model pollutants.

1. Introduction

Population growth, urbanization, industrialization, and climate change are leading to increasing global water demands [1]. Severe droughts affected 3 % of the global land area and the associated population from 1976 to 2005, a percentage that is expected to double by the end of the century [2]. During the droughts of 2018 and 2019, Central Europe had a deficit of about 112 and 145 Gt of water compared to an average year [3], which affected the agricultural, energy, and public water supply sectors and led to conflicts between sectoral water users [4]. Water reuse is considered an emerging solution to decrease the pressure on freshwater supplies and meet the water demand. The global water reuse capacity increased from 33.7 GL/day in 2010 to 54.5 GL/day in 2015 [5,6]. The decontamination of water by semiconductor photocatalysis is one of the Advanced Oxidation Processes (AOPs) that has received great interest over the past three decades [7–10] because it can remove pollutants dissolved in water in low concentrations, such as phenols [11], dyes [12], pesticides [13], pharmaceuticals [14], pathogens [15] that are difficult to remove by conventional water treatment processes.

TiO_2 has become the benchmark commercial semiconductor material as it is inexpensive, has long-term stability, and is relatively nontoxic [10]. However, the low quantum efficiency determined by the high recombination of photo-generated charge carriers and its application restricted to the UV region due to its wide band gap of around 3.2 eV decreases the overall efficiency of the photocatalytic process [16,17]. The reduction of TiO_2 has been previously used to extend the light absorption towards visible and near-infrared regions of the electromagnetic spectrum and to achieve superior photocatalytic activity compared to pristine TiO_2 [18–22]. The chemical reduction of TiO_2 with $NaBH_4$ led

---

* Corresponding authors.
E-mail addresses: anca.roibu@unitbv.ro (A. Roibu), andronic-luminita@unitbv.ro (L. Andronic).

https://doi.org/10.1016/j.jece.2024.112752
Received 10 December 2023; Received in revised form 29 March 2024; Accepted 7 April 2024

to materials of different colors such as blue, dark blue, light yellow, light grey and black [23–25] characterized by the presence of Ti^{3+} and oxygen vacancies, which were correlated to the observed narrower band gap and more efficient separation of the photo-generated charge carriers [26].

The photocatalysts obtained by the reduction of TiO_2 with $NaBH_4$ were predominantly tested under broad UV-Vis light spectrum lamps, such as halogen and Xe [23,27]. However, Liu et al. showed that the reduced TiO_2 is characterized by different quantum efficiencies between 455 and 530 nm depending on the concentration of Ti^{3+} and oxygen vacancies on its surface [28]. This demonstrates that further research is necessary to understand the relationship between the wavelength of the incident radiation and the structure/composition, optical properties, and photocatalytic activity of the materials. A single photocatalytic test typically requires a reaction time of several hours and 50–100 mL of polluted water when performed in a conventional batch photoreactor [22]. Consequently, screening the influence of multiple wavelengths on the activity of reduced TiO_2 along with the typical experimental conditions optimization (i.e., substrate and photocatalyst concentration, pH, and oxygen concentration) would require considerable time and consumption of reagents and photocatalytic material.

The investigation of wavelength influence on photocatalytic activity can be accelerated by high-throughput screening [29]. The standard approach in high-throughput screening consists of using multiwell-based plates characterized by liquid volumes such as 0.36 mL [30] and 5 mL per vial [31]. However, integrating flow microreactors in screening platforms presents several advantages such as high surface-to-volume ratio, effective photon transfer, and short diffusion lengths [32–36] leading to reaction times smaller than 15 min and reduced consumption of reagents due to their characteristic low volume and flow rate (90 μL, 100 μL/min [37] and 71 μL, 47–284 μL/min [38]). In addition, the ease of connecting microreactors to inline analytical techniques makes them more suitable for screening automation [39].

Catalyst screening in flow mode has been realized in channels characterized by dimensions ranging from 15 to 800 μm [40] [41]. TiO_2-based photocatalysts were previously introduced in the flow photoreactor as slurry or immobilized [42–45]. The photoreactors with immobilized photocatalysts are advantageous because no separation of catalyst particles is required, and when the supported photocatalyst is stable, multiple conditions can be tested on the same photocatalyst film, a benefit that is not attainable in the batch mode. While the activity and stability of deposited TiO_2 photocatalysts were extensively studied [46–50], only limited reports investigated the activity and stability of immobilized reduced TiO_2 [51,52].

Combining microreactors with additive manufacturing and LEDs as light sources has become increasingly attractive for setting up devices for testing photochemical reactions. 3D printing provides minimal design constraints, rapid prototyping, and high efficiency in materials consumption [53–55] and has been used to fabricate photo microreactors for water treatment using materials such as polylactic acid (PLA) [47,56], acrylonitrile butadiene styrene (ABS) [57], and resins [58]. The small size of LEDs and their large variety of emitting wavelengths from 265 to 730 nm allowed the design of compact light sources with multiple emission spectra that facilitated the screening of wavelength-dependent activity [59–61]. Hence, flow photoreactors manufactured by 3D printing, with immobilized photocatalysts, and irradiated by LEDs with narrow emission would offer the appropriate environment for studying the wavelength-dependent photocatalytic activity of reduced TiO_2 photocatalysts.

In this study, defective TiO_2 materials are prepared by chemical reduction with $NaBH_4$ and extensively characterized. Next, the pristine and reduced TiO_2 materials are tested as powders in a conventional batch photoreactor and immobilized as thin films in a 3D-printed photo microreactor for the photocatalytic degradation of imidacloprid (IMD). IMD is a pesticide with high toxicity, especially for bees, and has been banned for agricultural use in the EU and UK since 2018 [62–64]. However, it is still used for treating parasites of cats and dogs and was found to be one of the highest-risk compounds detected in London's waterways [64,65]. Moreover, imidacloprid can be considered a model compound for pollutants that are challenging to degrade due to its complex molecular structure. The influence of incident wavelength on the photocatalytic activity is investigated in batch and flow modes at three different irradiations, i.e., 395–400, 413, and 443 nm, provided by in-house developed LED light sources. To accelerate the screening in flow, a new testing methodology is proposed that consists of successive tests under various conditions (i.e., three illuminations and absence/addition of air gas) performed on the immobilized photocatalyst using a novel multi-wavelength rotating light source. The IMD degradation efficiencies determined in flow mode were compared with the values acquired in batch mode, and the stability of the photocatalysts in flow conditions was discussed.

2. Materials and methods

2.1. Materials preparation

The synthesis of reduced TiO_2 materials is performed by chemical reduction. A mass of 2 g of TiO_2 (P25/20, VP Aeroperl, Evonik), noted in this study as P25, was grounded with 1 g $NaBH_4$ (sodium borohydride, 99 %, VenPure, Acros Organics) and introduced in a covered porcelain crucible. The mixtures were heated for 30 min under an air atmosphere at temperatures ranging from 260 to 400 °C with a heating rate of 4 °C min^{-1}. To investigate the influence of reduction time, an additional material was obtained by heating the mixture for 3 h at 275 °C. The synthesized materials were removed from the oven, cooled down to room temperature, and washed with ethanol and deionized water several times while adjusting the pH of the solution with HCl (1 M) until pH=6–7. The filtered cake was dried at room temperature for 24 h and then in an oven at 50 °C and 40 mbar for 1 h. The obtained materials were noted as R-*X*-*Y*, in which *X* represents the reduction temperature and *Y* is the reduction time. After a preliminary activity study of the prepared materials as shown in Figure S1, the following materials were selected for further characterization and activity investigation: R-275–0.5 H, R-275–3 H, R-300–0.5 H, and R-400–0.5 H.

2.2. Materials characterization

The specific surface area and porosity of the prepared materials were obtained from N_2 adsorption-desorption isotherms measured using a physisorption analyzer (Tristar II Plus, Micromeritics) at −196 °C. Before N_2 adsorption, the analysed samples were degassed at 50 °C for 8 h. The specific surface area was determined by using the linear portion of the BET model and the pore diameter distribution using the Barrett-Joyner-Halenda (BJH) equation from the desorption isotherm.

The crystal structure of the samples was investigated using a powder X-ray diffractometer from Panalytical Empyrean equipped with an X-ray tube, Cu Kα cathode, and a PIXcel 3D detector.

The chemical composition of the samples was evaluated using a fully automated Thermo-Scientific X-ray Photoelectron Spectrometer using monochromated Al Kα radiation. A diffuse reflectance measurement using a UV-Vis spectrometer Jasco V-670 dual-beam UV-Vis/NIR spectrometer covering 200–1000 nm and Kubelka-Munk model were utilized to determine the band gap value of the materials from the reflectance measurements.

Transmission electron microscopy (TEM) images were carried out with a JEOL JEM-1400 Plus apparatus using an electron beam of 200 keV. Raman spectra were determined by using a microscopic confocal Jasco NRS-5100 Raman spectrometer in the range of 100–800 cm^{-1} with 532 nm excitation.

2.3. Photocatalytic testing in batch

Batch photocatalytic tests were carried out in a 60 mL glass vessel illuminated by an in-house built LED light source. The investigations were performed at ambient temperature (20–25 °C), however, the liquid temperature increased throughout the experiment for several photocatalysts. A glass cover was placed on top of the glass vessel to minimize water evaporation and increase pollutant concentration. Three light sources with maximal emissions at 400, 413, and 443 nm were used and placed at a distance of 1.1 cm from the glass cover and 2.4 cm from the initial liquid level. Each light source was operated at 9.4 W and consisted of 9 high-power LEDs equipped with 30° viewing angle lenses. The LEDs were placed on an aluminium heat sink and were cooled by water recirculation (see Figure S2 in ESI). The irradiance in the range of 200–1100 nm was measured for each light source using a UV-Vis spectrometer (AvaSpec-ULS2048CL-EVO-UA, Avantes) connected to an optical fiber (UVIR200–2-BX-FC/PC, Avantes) and a cosine corrector (CC-VIS/NIR, Avantes). The normalized spectral irradiance for each type of light source is depicted in Fig. 1b.

In a typical batch test, photocatalysts with a loading of 1 g/L were added into 50 mL IMD solutions (2.5 mg/L) with unmodified pH. While the environmental concentration of IMD in water was reported to vary between 10^{-6} to 0.3 ppm [66], the concentration of 2.5 ppm was chosen to enable a reliable comparison among materials with a wide range of activities, between the batch and flow screening modes, and to limit the influence of IMD adsorption and diffusion on degradation efficiency values.

The suspensions were magnetically stirred and kept in the dark for 30 min to establish adsorption equilibrium. The photocatalytic reactions were initiated by continuously irradiating the suspensions using the LED light source. Aliquots of 1 mL were typically collected every 30 min for 2 h, filtered with a syringe filter (PES, 0.45 μm), and analyzed by high-performance liquid chromatography (HPLC). The HPLC analysis was carried out using a Shimadzu LC- 20 ADsp instrument equipped with a C18-Macherey Nagel column, Nucleosil 5 μm, and a UV detector SPD-20A set at a wavelength of 270 nm. The mobile phase used was acetonitrile: water (70:30, v/v), the flow was set at 1.2 mL/ min, and the temperature at 40 °C. The degradation efficiency was calculated using the following equation:

$$\text{Degradation efficiency} = \frac{C_0 - C}{C_0} \times 100 \qquad (1)$$

where C_0 and C are the initial and the sampled concentration of IMD at a certain time, respectively.

2.4. Photocatalytic testing in flow

2.4.1. Photocatalyst immobilisation on glass plate

The powdered photocatalysts were deposited on soda lime glass plates (2.6 × 7.5 × 0.1 cm, Thermal Fisher) by spray coating. The coated area (8.7 cm^2) was kept constant among different samples by using a metal mask during the spraying process, characterized by a 6.7 × 1.3 cm window. Before the deposition, the glass plates were washed with a soapy solution, rinsed with deionized water, and sonicated in ethanol for 10 min. An ethanol suspension of the photocatalyst (7 g/L) was sonicated for 10 min and then sprayed on the glass support, which was heated to 150 °C.

The spraying was performed using a nozzle connected to a compressed air pump. Uniformly distributed films were obtained by applying multiple photocatalyst layers with a waiting period between coatings, followed by a drying time of 15 min at 150 °C (see Figure S3 in ESI). The total deposition time varied between 45 and 60 min. It was reported that reduced TiO_2 oxidizes at temperatures above 200 °C [28]. To ensure a proper comparison between the screening method implemented in batch and flow modes, prolonged thermal treatment and the calcination of immobilized films were avoided so that the oxidation and the modification of the optical and textural properties of the reduced photocatalysts are minimal compared to the powdered materials. The mass of the deposited photocatalyst was controlled by adjusting the volume of the sprayed photocatalyst suspension. The efficiency of material deposition on the glass plate varied between 6 % and 9 %. Efficiencies up to 40 % were achieved by decreasing the distance between the nozzle and the glass plate. However, it led to the formation of splatters, and the obtained films were mechanically unstable during the flow experiments.

For estimating the thickness of the photocatalyst film, it was assumed that the transmitted radiation through the film decreases exponentially as $I = I_0 \exp[-\alpha\delta]$, where I_0 is the incident light intensity at 365 nm measured through the glass plate without the film, I is the transmitted light intensity at 365 nm measured through the glass plate and the deposited film, and α is the absorption coefficient equal to 0.6264 μm^{-1} at 365 nm as previously reported [42,67]. The estimated values for the film thickness are 2.26, 1.95, and 1.87 μm for P25, R-275–0.5 H, and R-275–3 H, respectively. The transmittance, $T = I/I_0$, at 365 nm and the overall transmittance for the LED types used in this study are listed in Table S1 in ESI.

2.4.2. 3D printing of the flow photoreactor

The photo microreactor components were designed using SolidWorks 2016 (Dassault Systèmes) and the 3D models can be visualized in Fig. 2. Images of the 3D printed components are shown in Figure S4 in ESI. As can be seen, the flow photoreactor consists of a component A, which is the plate containing the reactor channel, and a component B, which contains the photoreactor window. The photocatalyst immobilized on the glass plate is introduced between the two plates. The 3D models were saved in STL file format and used as input data in the additive manufacturing process. Fused deposition modeling (FDM) is a material extrusion process [55] and was employed to manufacture components A and B using BCN3D Sigma X printer and PLA filament

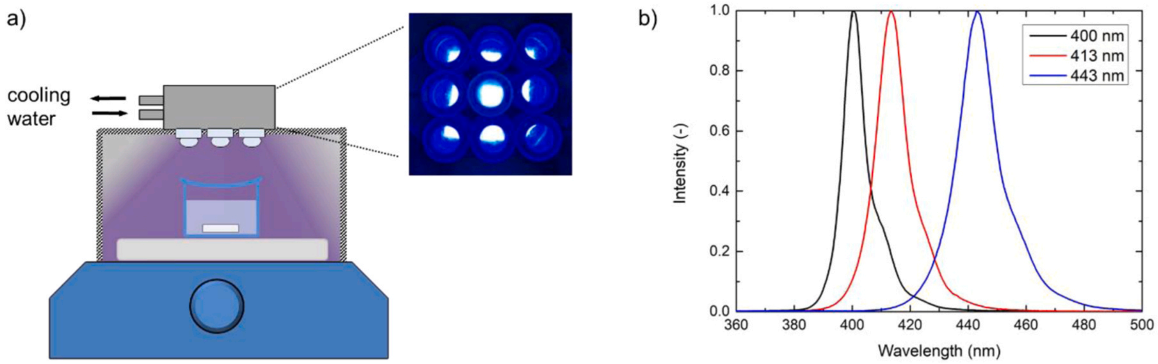

Fig. 1. (a) The schematic of the experimental setup used for batch photocatalytic tests and (b) spectral distribution of employed LED light sources.

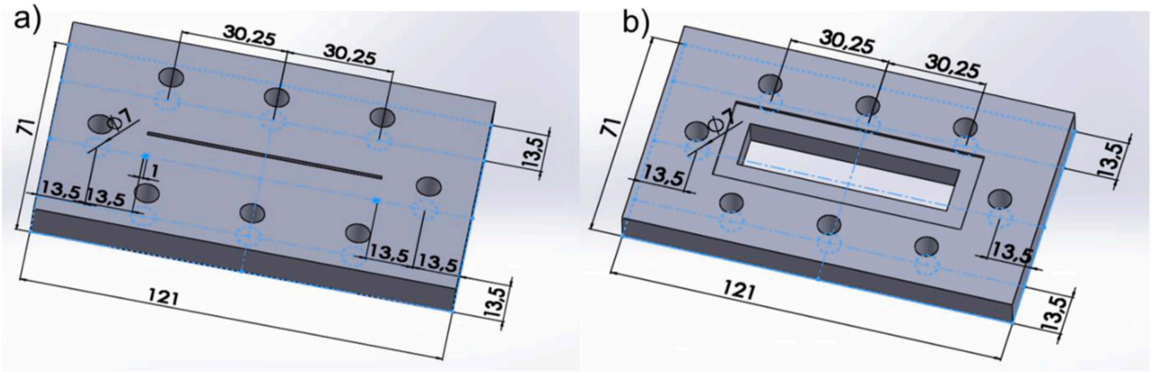

Fig. 2. (a) 3D Model of microreactor component A, the plate containing the photoreactor channel, and (b) 3D model of microreactor component B, the plate containing the photoreactor window.

with a diameter of 2.85 mm.

The software used to prepare the build platform for producing the models and to simulate the build time and material consumption was BCN3D Cura 3.4.1. The main manufacturing parameters were hotend of 0.4 mm, layer thickness of 0.2 mm, infill density of 60 %, build plate temperature of 60 °C, and extruder printing temperature of 210 °C. The manufacturing time was 8 h and 20 min for component A and 7 h and 35 min for component B.

The reactor channel has a length of 6.7 cm and a squared cross-section of 1 mm. The reactor window defines the illuminated area and is characterized by a length of 6.5 cm and a width of 1.5 cm. To avoid liquid leakage from the channel when it was covered with the glass plate, a thin silicone layer with the role of a sealing gasket was sprayed around the channel. In addition, two ports (NanoPort Kit, Upchurch Scientific) were glued on the opposite side of the 3D-printed plate A to connect its inlet and outlet to PTFE tubing (1/16" OD, 0.8 mm ID).

2.4.3. *Experimental setup for activity screening in flow*

The experimental setup used for the photocatalytic tests performed in flow is schematically represented in Fig. 3a and can be visualized in Figure S5 in ESI. The solution of IMD (2.5 mg/L) was conveyed through the flow photoreactor using a syringe pump (NE-501 OEM, New Era). The flow rate of the pump was controlled from the computer using WinPumpTerm software and was set to 3.5 mL/h. For the gas-liquid photocatalytic tests, a mass flow controller (MFC, EL-FLOW Select, Bronkhorst) was used to control the air flow rate of 1.75 mL/h. The liquid and the gas flows meet in a T-junction (Upchurch Scientific) and form a regular Taylor flow, which can be observed upon entering the microreactor. After exiting the microreactor, the length of the slugs and bubbles increases significantly, as the two-phase hydrodynamics are affected by (i) inlet and outlet geometry and (ii) the wettability of the PLA channel and the immobilized photocatalyst.

The pollutant solution was illuminated by an in-house developed LED light source. The light source consisted of three linear LED arrays, each containing 5 LEDs equipped with 30° viewing angle lenses placed on the separate sides of a water-cooled metal tube with a rectangular cross-section. The LEDs were grouped by the maximum emission wavelength as follows: (i) 395 nm, (ii) 413 nm, and (iii) 443 nm (Fig. 3b) and were operated at 5.4 W. The light sources were placed at a distance of 1.5 cm from the glass plate. The different LEDs location for batch and flow modes is assumed to have little effect on the comparison between the screening methods considering Figures S6-S7 in ESI.

For a fast alternation of the three types of illumination and, consequently, an accelerated wavelength-dependence screening, the light source was rotated until the desired LED array faced the microreactor window. The cooling system was not stopped or disconnected during the rotation of the light source. The pollutant solution exiting the flow photoreactor was collected and analyzed by HPLC.

3. Results and discussions

3.1. *Materials characterization*

As shown in Fig. 4a, the color of the reduced materials turned from

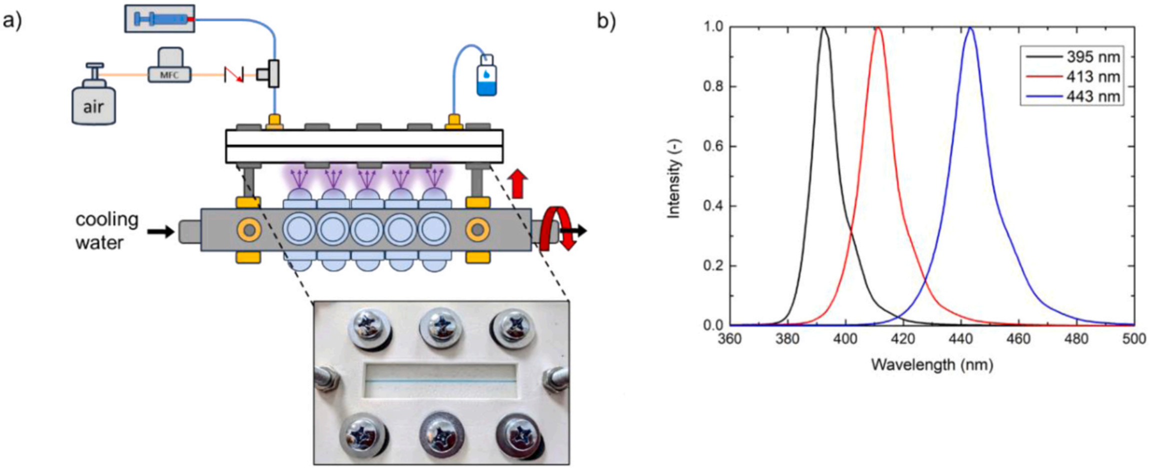

Fig. 3. (a) The schematic of the experimental setup used for flow photocatalytic tests. The inset image illustrates the front view of the assembled flow reactor in which the channel was highlighted using a blue-colored solution. (b) The spectral distribution of the LED light sources used in the flow photocatalytic tests.

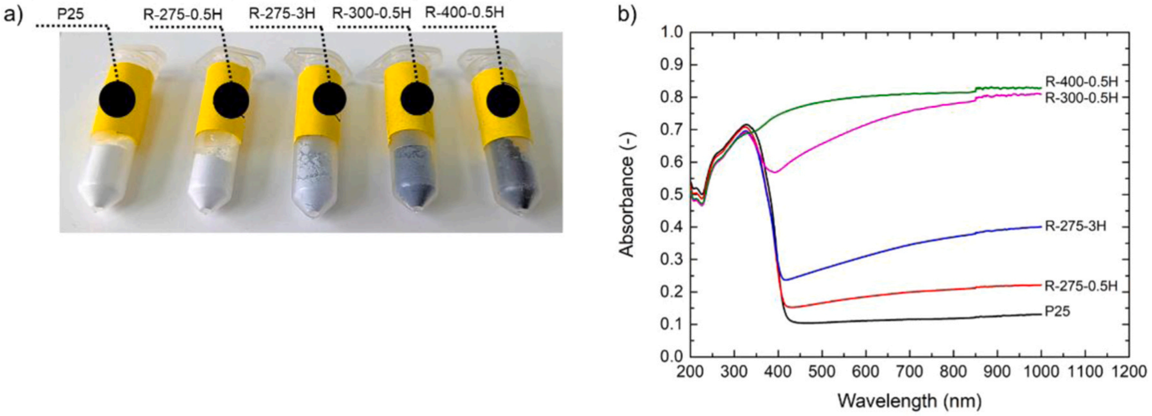

Fig. 4. (a) Images and (b) UV–vis diffuse absorbance spectra of pristine TiO_2 (P25) and reduced TiO_2 powders.

white to light gray and black by increasing the reduction temperature from 275 to 400 °C and the reduction time from 0.5 to 3 h. The corresponding diffuse absorption UV-Vis spectra are illustrated in Fig. 4b. The absorbance of the band 400–1000 nm significantly increases by raising the temperature and time of the reduction, while the absorbance below 400 nm experiences only a slight change irrespective of synthesis conditions. The absorption bands between 400 and 600 nm were attributed to color centers associated with oxygen vacancies, while the absorption above 600 nm originates from Ti-related (Ti^{n+}, n=2,3) color centers [68]. The increasing broad absorption between 400 and 1000 nm correlates well with the observed darkening of the reduced materials.

The optical band-gap energy, E_g, was determined from the measured reflectance spectra by combining Kubelka−Munk function and Tauc's relation as follows:

$$\left(F(R')h\nu\right)^{1/\gamma} = B\left(h\nu - E_g\right) \tag{2}$$

where $F(R') = \frac{(1-R')^2}{2R'}$ is the Kubelka−Munk function with $R' = \frac{R_{sample}}{R_{standard}}$, h is the Planck constant, ν is the photon's frequency, E_g is the band gap energy, and B is a constant [69,70]. The γ factor is equal to 1/2 for the direct transitions and 2 for indirect transitions. Direct and indirect transitions were considered and E_g was determined by intersecting the linear fit of the Tauc plots with the x-axis, as illustrated in Fig. 5.

The direct and indirect band gap energies for P25 were 3.23 and 2.96 eV, respectively, which are close to the previously reported values [71]. As can be observed from Table 1, there is only a slight difference between P25 and the reduced materials in terms of direct band gap energy, except for the most reduced material, R-400–0.5 H, for which a direct band gap of 1.56 eV was obtained. Generally, the defective TiO_2 obtained by reduction are considered indirect semiconductors [28, 72–74]. In this study, the indirect band gap energy decreased with the reduction temperature from 2.96 eV to 2.16 eV, as found for R-300–0.5 H. However, the indirect band gap for R-400–0.5 H was not determined because the linear fit of the Tauc plot could not be identified. This is expected when investigating defective, disordered, and amorphous materials that present broad absorbance at energies below E_g (i.e., Urbach tail) [69]. In this case, the Tauc plot method may not be suitable for determining the indirect band gap energy for R-400–0.5 H [75–77]. Nevertheless, it is evident that the higher reduction temperatures of 300 and 400 °C led to narrower bad gap energies compared to P25, which aligns with the observed darker color.

The BET-specific area was sensitive to the temperature and time of the reduction. As shown in Table 1, it significantly increased from 54 cm^2/g (P25) to 98 cm^2/g (R-400–0.5 H). The mean particle size measured by N_2 sorption decreases only slightly by reduction below 300 °C but becomes almost half compared to P25 by reduction at 400 °C. The same trend can be observed in the TEM images shown in Fig. 6a-d. The reduction at temperatures below 300 °C did not significantly affect the morphology. However, the chemical reduction at 400 °C led to smaller particles and the appearance of an amorphous phase, which was previously reported for samples with a high degree of reduction [25]. Amorphization of R-400–0.5 H was also confirmed by the XRD analysis shown in Fig. 7 and can be explained by the structural disorder induced by the created oxygen vacancies.

Fig. 8 shows the Raman spectra of P25 and reduced TiO_2 powders. The Raman bands at 140, 195, 395, 447, 515, and 637 cm^{-1} appear for P25 and materials reduced below 300 °C, and they correspond to the anatase phase. The band at 140 cm^{-1} broadens with the degree of

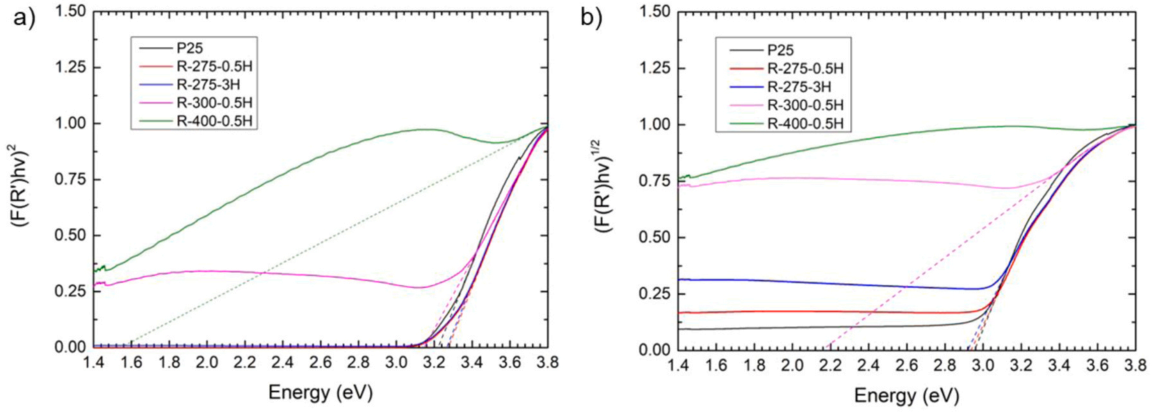

Fig. 5. Tauc plots for determining the (a) direct and (b) indirect band gap energies of pristine TiO_2 (P25) and reduced TiO_2 powders.

Table 1
Band gap energy determined from the Tauc plots and textural parameters obtained by N_2 adsorption-desorption measurement.

Samples	E_g -direct (eV)	E_g -indirect (eV)	S_{BET} (m^2/g)	Pore volume (cm^3/g)	Average pore size (nm)	Mean nanoparticle size (nm)
P25	3.23	2.96	54	0.64	43	110
R-275–0.5 H	3.28	2.94	56	0.45	29	106
R-275–3 H	3.27	2.92	57	0.45	30	105
R-300–0.5 H	3.15	2.16	58	0.52	35	103
R-400–0.5 H	1.56	-	98	0.30	16	61

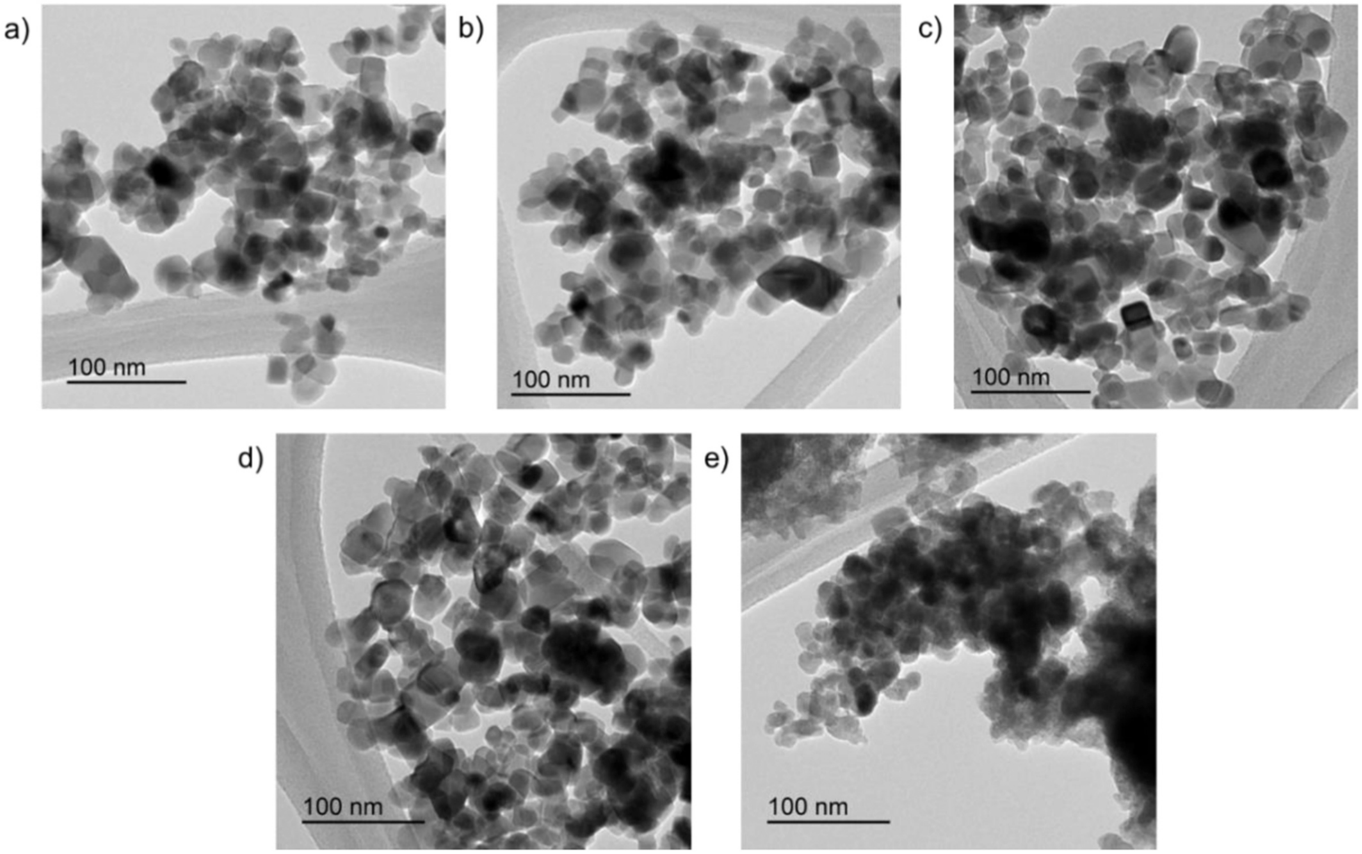

Fig. 6. TEM images of (a) pristine TiO_2 (P25) and reduced samples, (b) R-275–0.5 H, (c) R-275–3 H, (d) R-300–0.5 H, and (e) R-400–0.5 H.

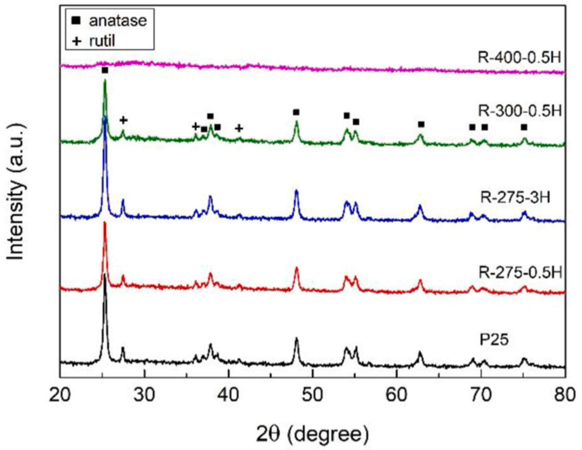

Fig. 7. XRD patterns of pristine TiO_2 (P25) and reduced TiO_2 powders.

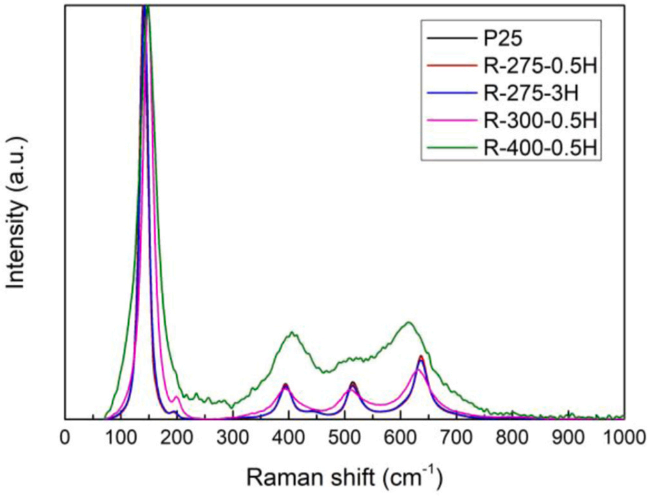

Fig. 8. Raman spectra of TiO_2 (P25) and reduced TiO_2 powders.

reduction and is blue shifted to 142 cm^{-1} for R-275–0.5 H and R-275–3 H and 149 cm^{-1} for R-300–0.5 H and R-400–0.5 H indicating the decrease of crystallite size and the presence of defects associated with surface oxygen vacancies [78].

In addition, R-400–0.5 H presents significant changes in the region of 300–800 cm^{-1} compared to the other analyzed powders. The bands 406 and 615 cm^{-1} correspond better to the rutile phase bands (441 and 615 cm^{-1} [79]). However, a phase transformation to rutile is in contradiction with the strong band of anatase at 149 cm^{-1} and missing rutile peaks in the XRD pattern of R-400–0.5 H. Similar modifications of Raman spectra were previously reported for Au/TiO_2 [80] and reduced graphene oxide/TiO_2 [79]. Non-stoichiometric phases, such as Magnéli type, could not be identified in the Raman spectrum of R-400–0.5 H, as the characteristic bands at 362, 449, 549, and 579 cm^{-1} were not distinguishable [79].

XPS spectra illustrated in Fig. 9 offer information about the chemical composition of the photocatalysts' surface and allow to identify the presence of Ti^{3+} species and oxygen vacancies. The peaks at 458.48 eV and 464.21 eV are assigned to Ti 2p 3/2 and Ti 2p 1/2 and are characteristic of P25. Following the chemical reduction, these peaks shifted to lower binding energies down to 458.39 eV and 464.10 eV for R-300–0.5 H, indicating the formation of Ti^{3+} [78]. For R-400–0.5 H, a shift is observed to higher binding energies, 458.78 eV and 464.61 eV, which could be attributed to the formation of Ti species with lower oxidation states, such as Ti^{2+}, due to over-reduction [78,81]. Fig. 9b shows the O 1 s spectra, from which the following types of surface oxygen species could be identified: (i) TiO_2 lattice oxygen species, $O_{TiO2\ lattice}$, at 529.7–530.3 eV (ii) surface adsorbed oxygen species (e.g. hydroxyl), O_{ads}, at 530.6–531.5 eV and (iii) chemically bonded water, O_{water}, 531.5–532.8 eV [78]. The presence of hydroxyl group was previously correlated with surface defects and oxygen vacancies [82,83].

The fraction of $O_{TiO2\ lattice}$ is 88–90 %, the fraction of O_{ads} is around 6–8 %, and the fraction of O_{water} is around 3–4 %, for P25 and the materials reduced below 300 °C. However, for R-400–0.5 H, the decreased fraction of oxygen in the lattice $O_{TiO2\ lattice} = 53$ %, and the increased fraction of adsorbed oxygen species $O_{ads} = 34$ % and $O_{water} = 13$ % proves that a high content of surface defects and oxygen vacancies characterized this material.

From the characterization results, it can be concluded that the high-temperature chemical reduction at 400 °C significantly affected the properties of TiO_2. In addition, the elemental composition measured by XPS and listed in Table 2 reveals that the ratio O:Ti for R-400–0.5 H is 1.6 times higher than for P25, probably due to adsorbed oxygen species. Moreover, R-400–0.5 H is the only material that contains Na and B, despite the fact that a similar washing procedure was applied to all reduced materials. The elimination of Na and B was less efficient for this material, probably due to its high specific surface area or sintering occurring at 400 °C.

3.2. Photocatalytic activity

The photocatalytic activity for IMD degradation of P25 and reduced TiO_2 was investigated in batch mode at 400, 413, and 443 nm. The photoreactor system ensured reproducible results as the average standard deviation for 2 replicates over the 2 h was ±3 % for R-275–0.5 H at 400 nm and ±0.6 % for R-400–0.5 H at 443 nm. Fig. 10a-d show that the photocatalytic activity for the investigated materials generally decreases by increasing the irradiating wavelength. At 400 and 413 nm,

Table 2
Elemental composition of the powdered samples measured by XPS.

Sample	Ti	O	C	Na	B	O:Ti
P25	22.96	55.93	21.13	0	0	2.44
R-275–0.5 H	22.90	56.14	20.96	0	0	2.45
R-275–3 H	22.11	56.76	21.12	0	0	2.57
R-300–0.5 H	22.47	56.12	21.4	0	0	2.50
R-400–0.5 H	13.93	55.79	18.51	1.97	9.8	4.01

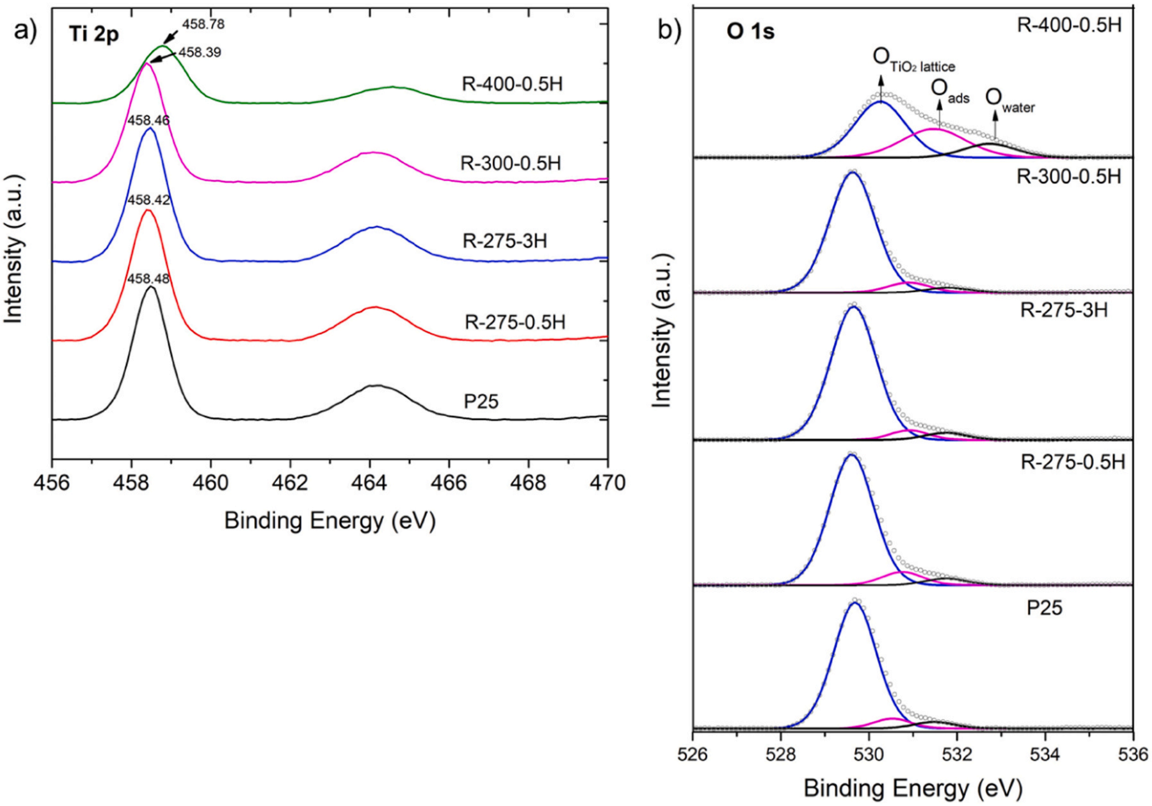

Fig. 9. (a) Ti 2p and (b) O 1 s XPS spectra for TiO_2 (P25) and reduced TiO_2 powders.

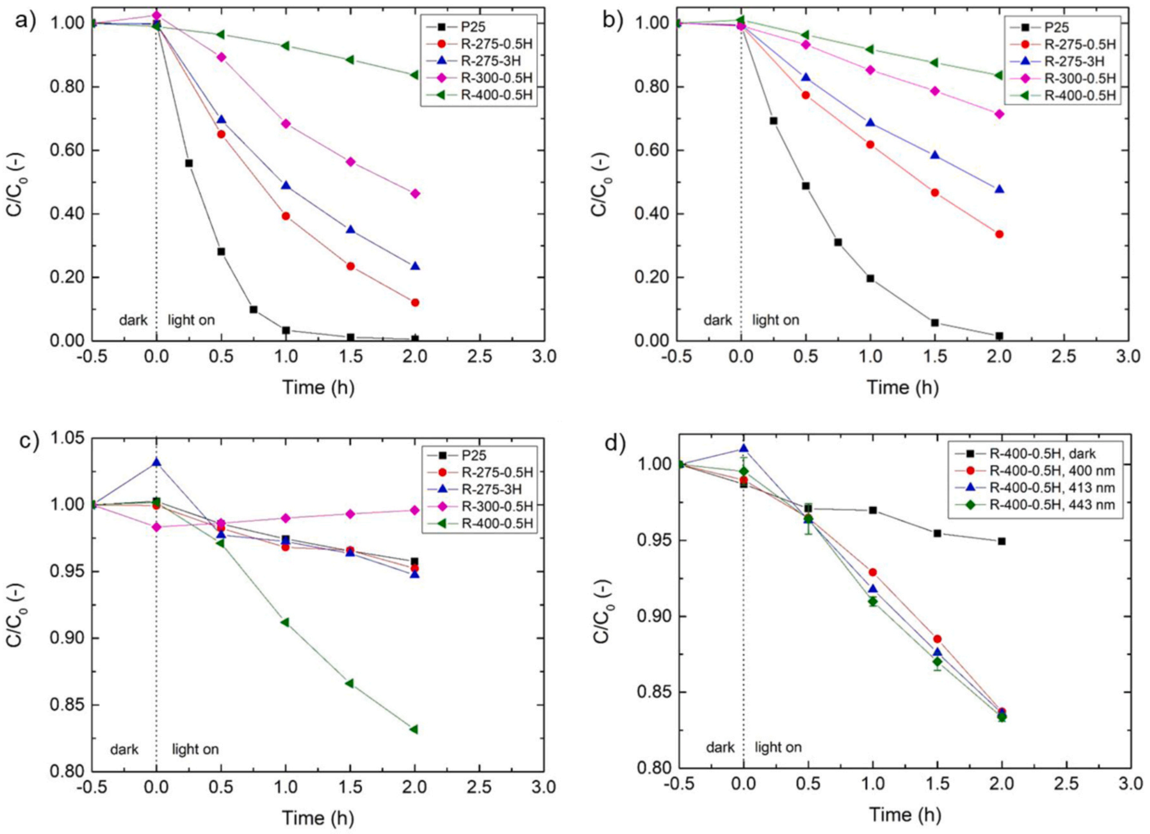

Fig. 10. The photocatalytic degradation of IMD in the presence of P25 and reduced TiO_2 powders in (a) batch at 400 nm, (b) batch at 413 nm, (c) batch at 443 nm, and (d) batch at 400, 413, and 443 nm in the presence of R-400–0.5 H.

P25 exhibits the highest photocatalytic activity among the tested photocatalysts, leading to full degradation of IMD after 2 h. The photocatalytic activity of the reduced TiO_2 materials at 400 and 413 nm decreased in the order of R-275–0.5 H> R-275–3 H> R-300–0.5 H> R-400–0.5 H, which correlates with increasing the degree of TiO_2 reduction. However, as can be seen from Fig. 10c, at 443 nm there is negligible photocatalytic activity for P25, and the majority of the reduced materials. R-400–0.5 H was the only active photocatalyst, leading to a degradation efficiency of 16.8 % at 443 nm after 2 h. The increasing IMD concentration as a function of time for R-300–0.5 H at 443 nm can be explained by low activity and water evaporation, which is followed by condensation on the glass cover. As can be observed in Table S2 in ESI, the liquid temperature increased up to 42.3 °C after 2 h because of the strong visible-light absorption by R-300–0.5 H, followed by the non-radiative recombination of charge carriers. In comparison, the liquid temperature was lower by 9 °C in the case of R-275–3 H. The liquid temperature reached 44.5 °C after 2 h in the case of R-400–0.5 H, which shows that the elevated liquid temperature did not lead to the observed IMD degradation in the presence of R-400–0.5 H. As shown in Fig. 10d, the photocatalytic activity of R-400–0.5 H slightly increases by changing the irradiation wavelength from 400 to 443 nm.

Because IMD adsorption in the dark did not exceed 5 %, and increasing the LEDs power at 400 nm improved the degradation efficiency, as illustrated in Fig. 11, it was concluded that the activity of R-400–0.5 H is light-driven. The lower photocatalytic activity for the reduced TiO_2 materials compared to P25 at 400 and 413 nm could be explained by the higher concentration of oxygen vacancies in the bulk compared to the surface [84–86]. While the observed activity of the photocatalyst prepared at 400 °C at 443 nm could be determined by the significantly higher content of defects, this is unexpected. The high degree of reduction is commonly associated with lower photocatalytic activity when irradiated with UV-Vis light sources, the defects acting as recombination centers [25,85]. However, the significant changes in the textural properties and crystalline structure and the presence of Na and B in the chemical composition could play a role in the different photocatalytic activity observed at 443 nm compared to the other reduced materials.

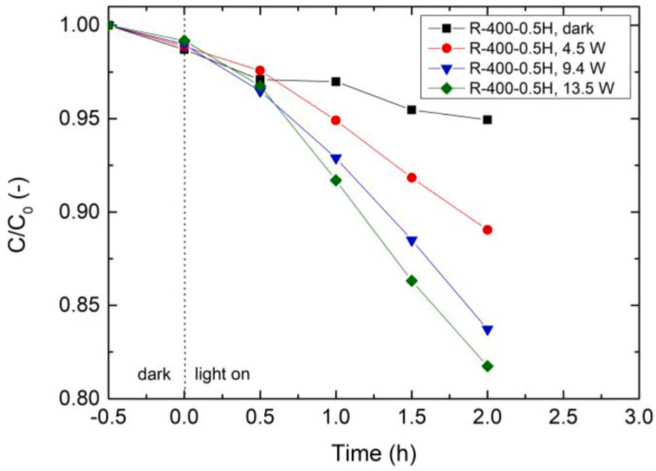

Fig. 11. Influence of LEDs power at 400 nm on IMD degradation in the presence of R-400–0.5 H.

While the activity of the TiO_2 reduced at 400 °C does not exhibit a significant performance, it is interesting to observe that its activity is generally maintained (a slight increase of 2 % at 1 h) between 380 and 480 nm, in contrast to the other materials investigated in this work.

Andronic et al. reported that the degradation rate of IMD in the presence of TiO_2 prepared by sol-gel method and reduced with $NaBH_4$ at 350 °C decreased by 50 % when changing the irradiation domain from UV (340–400 nm) to UV–visible (20 % of 340–400 nm and 80 % of 400–700 nm) [87]. Similarly, Bi et al. reported that the activity of reduced TiO_2 prepared by annealing at 500 °C for NO oxidation decreased by 50 % when increasing the irradiating wavelength from UV (365 nm) to visible range (white LED) [74]. The employed visible light sources, UV-Vis lamp and white LED, are characterized by a wide emission spectrum and the influence of the irradiating wavelength above 400 nm was not clear. However, Liu et al. showed that for a reduced TiO_2, the quantum efficiency decreased by increasing the wavelength from 455, to 470, and then to 530 nm. By applying a thermal treatment at 300 °C to the reduced photocatalyst, the apparent quantum efficiency changed as follows 530 nm > 455 nm > 470 nm [28]. The authors attributed the change in activity to the concentration of Ti^{3+} and oxygen vacancies on the surface. These observations indicate that further investigations focused on wavelength-dependent activity in the visible-light domain could bring more clarity about the visible light activity of reduced TiO_2, and therefore, improvement of the photocatalytic processes driven by solar light.

In the next step, the wavelength-dependent screening was performed in the flow photoreactor at 395, 413, and 443 nm for the selected photocatalysts: P25, R-275–0.5 H, and R-275–3 H. While the photocatalyst R-400–0.5 H exhibited an interesting wavelength-dependent activity, the photocatalyst R-400–0.5 H showed a degradation efficiency of 3.5 % after 30 min in the batch mode. Therefore, we estimate that in the flow photoreactor, the degradation efficiency would not exceed this value at the investigated residence time, making it difficult to observe the influence of various reaction conditions. For a reliable analysis of R-400–0.5 H photocatalytic activity in flow mode, a microreactor equipped with a longer channel would be required.

The screening in flow was performed for the same immobilized photocatalyst in two steps: in single-water phase and air-water two-phase flow. Fig. 12 illustrates the IMD degradation over immobilized P25 in function of operating time. The first step consisted of IMD adsorption in the dark at the liquid flow rate of 3.5 mL/h, followed by successive illumination at 395, 413, and 443 nm performed at the liquid flow rate of 3.5 mL/h, which corresponds to a residence time of 1.1 min. At the end of the first step, the stability of photocatalytic activity was tested by measuring the IMD degradation at 395 nm for the second time. In the second step, air gas was introduced in the flow photoreactor to investigate the effect of added oxygen near the photocatalytic film and of mixing on activity and stability. In the air-water flow, the total flow rate was kept at 3.5 mL/h, and the flow rate ratio air:water was 1:1. At the end of the second step, the IMD degradation was measured for the third time in the single water phase at 395 nm. From Fig. 12, it can be noted that IMD degradation over immobilized P25 was sensitive to all operating conditions, reached a maximum of 47.8 % in the air-water flow at 395 nm, and was relatively stable during 405 min of operation.

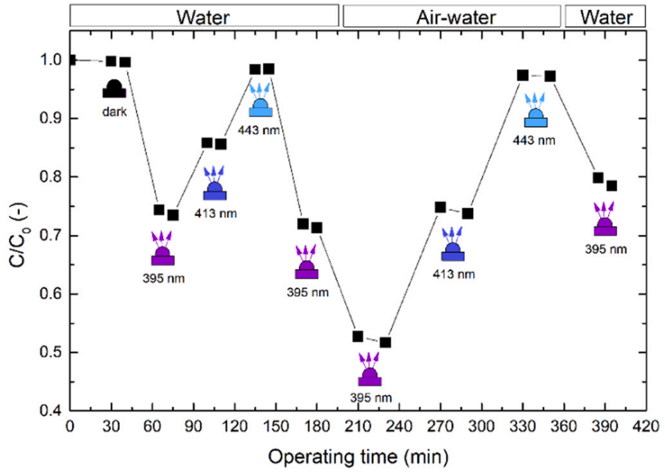

Fig. 12. The photocatalytic degradation of IMD in flow over immobilized P25 . The liquid flow rate in single water phase was 3.5 mL/h, and the total flow rate in air-water two-phase flow was 3.5 mL/h, where the liquid and gas flow rates were equal to 1.75 mL/h.

Fig. 13a compares the IMD degradation efficiency obtained in batch at 30 min and in flow mode at 1.1 min and different illuminations for P25, R-275–0.5 H, and R-275–3 H. The influence of the photocatalyst and irradiation on IMD degradation that was captured by the screening in flow mode matched well with the observations acquired in batch-mode. Moreover, IMD degradation in the water was around 10 times faster in the flow-mode at 395 nm/400 nm and around 7 times faster at 413 nm compared to batch-mode experiments. The degradation efficiency at 443 nm was low for the selected photocatalysts in both batch and flow-modes. By adding air gas, the degradation efficiency at 395 and 413 nm improved 1.8 times for P25, 2.7 times for R-275–0.5 H, and 2.1–2.4 times for R-275–3 H, compared to the water flow.

The influence of air gas was different for each investigated photocatalyst. It can be explained by (i) different effects of oxygen as a scavenger, (ii) development of activation/deactivation phenomena during operation, and (iii) different gas-liquid hydrodynamics in the reactor channel caused by the different wettability of the photocatalytic films. As shown in Figure S11 in ESI, a simple glass plate was used to observe the gas-liquid flow pattern. Due to the different wettability of PLA and glass plate, the Taylor flow was distorted, leading to faster gas bubbles and slower liquid slugs, which could translate into longer liquid residence times. Previously it was reported that surface hydrophilicity decreases by increasing the reduction degree of TiO_2 [86], therefore, the wettability of each investigated photocatalyst is important when performing screening using gas-liquid flows.

Fig. 13b illustrates the stability of the photocatalytic activity at 395 nm for P25, R-275–0.5 H, and R-275–3 H at different moments during the photoreactor operation (1st, 2nd, and 3rd tests). In the case of P25 and R-275–0.5 H, an increase of IMD degradation was observed in the 2nd test compared to the 1st test: from 26 % to 28.4 % and from 14.7 % to 22.6 %, respectively. This activation was attributed to the adsorption of the resulting products on the photocatalyst surface, as reported by Adamek et al [46].

After operating the photoreactor using the air-water flow, IMD degradation over P25 and R-275–0.5 H decreased to 20.1, and 21.4 %, respectively. P25 shows the largest activity decrease, probably due to the physical degradation of the thin film (see Figure S10). Notably, the reduced TiO_2, R-275–3 H, was the most stable photocatalyst, providing a constant IMD degradation efficiency of around 10 %. The higher stability of R-275–3 H could be explained by the lower amount of generated products that are adsorbed on the photocatalyst surface.

In addition to the expected higher rate of IMD degradation, screening in the flow benefits from reduced materials consumption. The flow photoreactor required 46 mg of photocatalyst to investigate 6 wavelength-dependent conditions and a polluted water volume of less than 20 mL as shown in Table 3. In comparison, a batch screening test consumed 50 mL of polluted water, which could provide only reaction time-dependent information. Due to the smaller footprint of the reactor channel, the light source operated at 5.4 W in flow, compared to the batch photoreactor, which required 9.4 W. Considering the entire time for a screening experiment, it would result in an energy consumption of 36.5 Wh in continuous flow-mode and 18.8 Wh in batch-mode. The water recirculation and cooling system was the largest energy consumer. However, the consumed energy could not be quantified as the cooling of water, which implied a fan turning on when exceeding 22 °C varied depending on the room temperature and the amount of heat produced by the light source. Nevertheless, the water cooling was less intense for the flow experiments due to the lower light source power of 5.4 W. Even though the photoreaction times are shorter (1.1 min vs 30 min), the

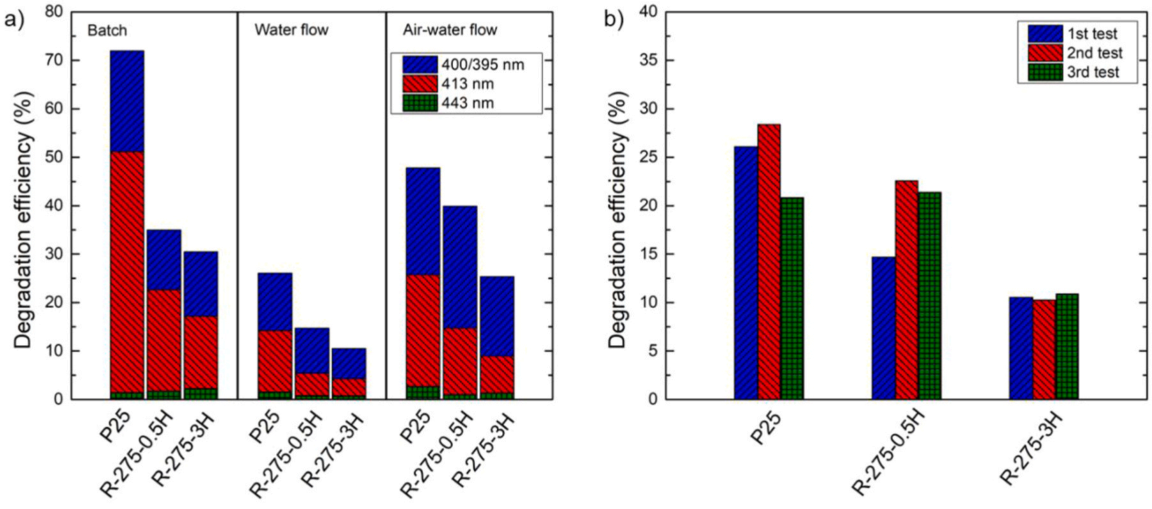

Fig. 13. (a) IMD degradation efficiency at different irradiating wavelengths in batch-mode after 30 min, single water phase in flow photoreactor at the residence time of 1.1 min, and air-water flow in flow photoreactor at an estimated residence time of 1.1 min. (b) The stability of IMD degradation efficiency in the single water phase at 400 nm and the residence time of 1.1 min.

Table 3
Comparison between the batch and flow approaches for a single screening experiment in terms of materials and energy consumption.

Parameter	Batch	Flow
Number of screened conditions	4–6	6
Parameter investigated	illumination time	illumination wavelength, air gas presence
Photoreactor operating time	120 min	405 min
Catalyst mass	50 mg	~46 mg
Polluted water volume	50 mL	17.2 mL
Light source energy	18.8 Wh	36.5 Wh

total screening time in flow-mode was increased to 405 min by the waiting time required to reach the steady state and to collect the samples for HPLC analysis. The screening throughput and energy consumption could be improved by using on-line analytics, such as UV-Vis spectroscopy. The sample collection time for the single-phase flow was 10 min and 20 min for the two-phase case. Integrating an online monitoring tool would decrease the screening time for the same conditions from 405 to 160 min.

Moreover, the volume of polluted water would decrease from 17.2 to 8.2 mL, and the energy consumption by the light source would go down to 14.1 Wh. At the moment, batch screening is the conventional screening method due to its simple operation and setup, which implies a lamp, a beaker, and a stirrer, and the reliable acquired experimental data (*i.e.*, free of mass transfer limitations). On the other hand, continuous-flow photocatalysis requires a larger investment in specialized equipment such as pumps, tubing, and appropriate connections, as well as interdisciplinary knowledge about film deposition, reactor design, and transport phenomena. Nevertheless, with the commercial flow photoreactors and inline analytics becoming more accessible and the increased awareness and efforts for transitioning towards sustainable processes, the proposed methodology is a promising approach for accelerating the photocatalysts screening while minimizing the consumption of photocatalysts and water contaminated with model pollutants.

Finally, we compared the performance of the batch and flow photoreactors used in this study with the performance of other reported photoreactors as illustrated in Table 4. Similar to our results, the degradation rate of pollutants is several times higher in flow photoreactors compared to the batch systems due to the higher photocatalyst concentration (photocatalyst mass per liquid volume) in the case of film-based photoreactors and the reduced light attenuation across the channel in the case of the slurry photoreactors due to the shorter optical pathlength. Moreover, it is well known that the microreactors characterized by smaller channel heights (i.e. 0.1–0.3 mm) are more advantageous. However, we chose a channel height of 1 mm to achieve reproducible manufacturing of the reactor channel, considering that the resolution of the 3D printer is 0.1 mm, and to accommodate potential slight modifications of the photoreactor geometry during multiple rapid changes of the photocatalytic film. As can be observed in Table 4, only a single other flow photoreactor is designed with a straightforward replaceable film [88]. In addition, the flow photoreactor reported in this study is the only one equipped with a light source containing multiple pseudo-monochromatic optical outputs, allowing the rapid investigation of the wavelength influence on the visible-light-activated photocatalytic materials.

4. Conclusions

This study focuses on extending TiO_2 absorption to the visible domain and screening its wavelength-dependent photocatalytic activity for pesticide removal. Firstly, grey to black photocatalysts were prepared by chemical reduction of the commercially available TiO_2 P25 at temperatures between 275 and 400 °C. The obtained materials were characterized by an increased specific surface area and lower direct (up to 1.56 eV) and indirect band gap energies (up to 2.16 eV). A considerable content of oxygen vacancies was achieved, as shown from XPS analysis, especially at the highest reduction temperature of 400 °C. Interestingly, this reduction temperature led to an amorphous TiO_2-based photocatalyst, as indicated by XRD analysis.

Even though the reduced TiO_2 materials were characterized by broad light absorption in UV, visible, and infrared regions, the pristine TiO_2 (P25) was more active for the degradation of imidacloprid at 400 nm and 413 nm. However, at 443 nm and in the batch photoreactor, the material reduced at 400 °C exhibited the highest degradation efficiency of 16.8 % compared to only 4.2 % as measured for P25. Therefore, the photocatalytic activity predominantly decreased by increasing the radiation wavelength, except for R-400–0.5 H which exhibited a constant degradation efficiency. Therefore, this study shows the importance of studying the influence of irradiating wavelength on the activity together with the textural and optical properties.

Table 4
Comparison of reported performance for batch and flow photo (micro)reactors applied in photocatalytic degradation of organic pollutants in water over TiO_2 P25. IMD is imidacloprid, HA represents humic acids, RhB is rhodamine B, MB is methylene blue, and CA is clofibric acid.

Pollutant (C_0)	Batch				Flow				Ref.
	C_{TiO2}, type	Reactor, (Volume)	Light source (Wavelength)	Degradation efficiency, time	C_{TiO2}, type	Reactor (Volume, dimensions)	Light source (Wavelength)	Degradation efficiency, time	
IMD (2.5 ppm)	1 g/L, slurry	glass vessel (50 mL)	LED (400 nm) LED (413 nm) LED (443 nm)	97 %, 60 min 80 %, 60 min 2.6 %, 60 min	5.3 g/L, replaceable film	microreactor (0.6 mL, 1 × 1 mm)	LED (395 nm) LED (413 nm) LED (443 nm)	26 %, 1.1 min 14 %, 1.1 min 2.7 %, 1.1 min	This work
HA (10 ppm)	0.1 g/L, slurry	glass vessel (200 mL)	LED (365 nm)	53 %, 60 min	0.1 g/L, slurry	microreactor (1.7 mL, 1 mm)	LED (365 nm)	20 %, 1.7 min	[89]
RhB (15 ppm)	0.06 g/L, replaceable film	glass vessel (14 mL)	halogen lamp (365 nm)	33 %, 60 min	5.4 g/L, film with epoxy sealing	microreactor (0.15 mL, 5 × 0.3 mm)	LED (365 nm)	32 %, 1.5 min	[90]
MB (9.6 ppm)	C_{TiO2}, replaceable film	PDMS container (3 mL)	solar simulator	60 %, 60 min	33·C_{TiO2}, fixed film	microreactor (0.09 mL, 18 × 0.1 mm)	solar simulator	75 %, 0.9 min	[37]
CA (20 ppm)	0.004 g/L, fixed film	glass vessel (54 mL)	halogenated mercury lamp	20 %, 60 min	0.9 g/L, replaceable film	microreactor (0.2 mL, 20 × 0.18 mm)	UV lamps (365 nm)	60 %, 1 min	[88]

To accelerate the activity screening and reduce materials consumption, a flow microreactor designed in-house and manufactured by 3D printing was paired with a novel multi-wavelength rotative LED light source. The most active materials P25, R-275–0.5 H, and R-275–3 H were immobilized as uniform thin films on glass plates which were integrated into the microreactor. Multiple conditions were investigated such as irradiating wavelength, presence of air gas, and stability at different operating times.

In flow, the rate for IMD degradation was higher than in the batch photoreactor, but the degradation efficiency was limited by the relatively short residence time of 1.1 min which was not sufficient for testing the most interesting material, R-400–0.5 H. The maximal degradation efficiency achieved for P25 at 395 nm and single-phase flow was 28.4 %, compared to full conversion after 2 h in batch at 400 nm. The addition of the gas phase in the flow photoreactor increased the degradation efficiency to 47.8 % at the same irradiating wavelength. Most importantly, the influence of the wavelength and photocatalyst on IMD degradation observed in microreactor correlated well with the observations acquired in batch, proving the reliability of the knowledge gained by screening in flow, even though the tests were performed on a single immobilized photocatalyst. In addition, the thin films showed relatively good stability in terms of photocatalytic degradation efficiency, with an interesting activity increase after 150 min of operation.

This study showed that performing successive tests on the same immobilized photocatalyst using a rotating LED light source is a promising method to accelerate the screening of photocatalytic activity at different visible-light wavelengths while improving the sustainability of the screening process by reducing the consumption of photocatalytic material and reagents. To strengthen the benefits of screening in flow, the microreactor should be coupled with inline analytics. Moreover, future research should focus on (i) improving the photocatalytic activity of reduced TiO_2 by exploring the influence of the amorphous phase and the elements Na and B, (ii) understanding and controlling the factors affecting the stability of thin films while operating in continuous flow and (iii) designing flow photoreactors characterized by improved degradation efficiencies. The latter can be achieved by either increasing the length of the channel to reach longer residence times or by decreasing the height of the channel to obtain a larger catalyst mass/liquid volume ratio.

CRediT authorship contribution statement

Razvan Udroiu: Writing – review & editing, Writing – original draft, Methodology, Investigation. **Joaquin Silvestre-Albero:** Writing – review & editing, Supervision, Methodology, Funding acquisition. **Coset Abreu-Jaureguí:** Writing – review & editing, Investigation, Data curation. **Anca Roibu:** Writing – review & editing, Writing – original draft, Methodology, Investigation, Funding acquisition, Data curation, Conceptualization. **Luminita Andronic:** Writing – review & editing, Supervision, Resources, Methodology, Funding acquisition, Conceptualization.

Declaration of Competing Interest

The authors declare that they have no known competing financial interests or personal relationships that could have appeared to influence the work reported in this paper.

Data Availability

Data will be made available on request.

Acknowledgments

This work was supported by the Romanian Ministry of Research, Innovation and Digitization, CNCS−UEFISCDI (grant PN-III-P1–1.1-PD-2021–0387), MINECO (PID2019–108453GB-C21) and MCIN/AEI/10.13039/501100011033 and EU "NextGeneration"/PRTR (Project PCI2020–111968/ERANET-M/3D-Photocat).

Appendix A. Supporting information

Supplementary data associated with this article can be found in the online version at doi:10.1016/j.jece.2024.112752.

References

[1] OECD, OECD Environmental Outlook to 2050: The Consequences of Inaction, Paris, 2012.

[2] Y. Pokhrel, F. Felfelani, Y. Satoh, J. Boulange, P. Burek, A. Gädeke, D. Gerten, S. N. Gosling, M. Grillakis, L. Gudmundsson, N. Hanasaki, H. Kim, A. Koutroulis, J. Liu, L. Papadimitriou, J. Schewe, H. Müller Schmied, T. Stacke, C.-E. Telteu, W. Thiery, T. Veldkamp, F. Zhao, Y. Wada, Global terrestrial water storage and drought severity under climate change, Nat. Clim. Chang 11 (2021) 226–233, https://doi.org/10.1038/s41558-020-00972-w.

[3] E. Boergens, A. Güntner, H. Dobslaw, C. Dahle, Quantifying the Central European Droughts in 2018 and 2019 With GRACE Follow-On, Geophys Res Lett. 47 (2020) e2020GL087285, https://doi.org/10.1029/2020GL087285.

[4] V. Blauhut, M. Stoelzle, L. Ahopelto, M.I. Brunner, C. Teutschbein, D.E. Wendt, V. Akstinas, S.J. Bakke, L.J. Barker, L. Bartošová, A. Briede, C. Cammalleri, K. C. Kalin, L. De Stefano, M. Fendeková, D.C. Finger, M. Huysmans, M. Ivanov, J. Jaagus, J. Jakubínský, S. Krakovska, G. Laaha, M. Lakatos, K. Manevski, M. Neumann Andersen, N. Nikolova, M. Osuch, P. van Oel, K. Radeva, R. J. Romanowicz, E. Toth, M. Trnka, M. Urošev, J. Urquijo Reguera, E. Sauquet, A. Stevkov, L.M. Tallaksen, I. Trofimova, A.F. Van Loon, M.T.H. van Vliet, J.-P. Vidal, N. Wanders, M. Werner, P. Willems, N. Živković, Lessons from the 2018–2019 European droughts: a collective need for unifying drought risk management, Nat. Hazards Earth Syst. Sci. 22 (2022) 2201–2217, https://doi.org/10.5194/nhess-22-2201-2022.

[5] N. Voulvoulis, Water reuse from a circular economy perspective and potential risks from an unregulated approach, Curr. Opin. Environ. Sci. Health 2 (2018) 32–45, https://doi.org/10.1016/J.COESH.2018.01.005.

[6] Z. Chen, H.H. Ngo, W. Guo, A critical review on the end uses of recycled water, Crit. Rev. Environ. Sci. Technol. 43 (2013) 1446–1516, https://doi.org/10.1080/10643389.2011.647788.

[7] O. Legrini, E. Oliveros, A.M. Braun, Photochemical processes for water treatment, Chem. Rev. 93 (1993) 671–698, https://doi.org/10.1021/cr00018a003.

[8] A. Mills, R.H. Davies, D. Worsley, Water purification by semiconductor photocatalysis, Chem. Soc. Rev. 22 (1993) 417–425, https://doi.org/10.1039/CS9932200417.

[9] M.N. Chong, B. Jin, C.W.K. Chow, C. Saint, Recent developments in photocatalytic water treatment technology: a review, Water Res. 44 (2010) 2997–3027, https://doi.org/10.1016/j.watres.2010.02.039.

[10] S.K. Loeb, P.J.J. Alvarez, J.A. Brame, E.L. Cates, W. Choi, J. Crittenden, D. D. Dionysiou, Q. Li, G. Li-Puma, X. Quan, D.L. Sedlak, T. David Waite, P. Westerhoff, J.-H. Kim, The technology horizon for photocatalytic water treatment: sunrise or sunset? Environ. Sci. Technol. 53 (2019) 2937–2947, https://doi.org/10.1021/acs.est.8b05041.

[11] S. Ahmed, M.G. Rasul, W.N. Martens, R. Brown, M.A. Hashib, Heterogeneous photocatalytic degradation of phenols in wastewater: a review on current status and developments, Desalination 261 (2010) 3–18, https://doi.org/10.1016/j.desal.2010.04.062.

[12] A. Ajmal, I. Majeed, R.N. Malik, H. Idriss, M.A. Nadeem, Principles and mechanisms of photocatalytic dye degradation on TiO_2 based photocatalysts: a comparative overview, RSC Adv. 4 (2014) 37003–37026, https://doi.org/10.1039/C4RA06658H.

[13] S. Kanan, M.A. Moyet, R.B. Arthur, H.H. Patterson, Recent advances on TiO_2-based photocatalysts toward the degradation of pesticides and major organic pollutants from water bodies, Catal. Rev. 62 (2020) 1–65, https://doi.org/10.1080/01614940.2019.1613323.

[14] K.S. Varma, R.J. Tayade, K.J. Shah, P.A. Joshi, A.D. Shukla, V.G. Gandhi, Photocatalytic degradation of pharmaceutical and pesticide compounds (PPCs) using doped TiO_2 nanomaterials: a review, Water-Energy Nexus 3 (2020) 46–61, https://doi.org/10.1016/j.wen.2020.03.008.

[15] P.V. Laxma Reddy, B. Kavitha, P.A. Kumar Reddy, K.-H. Kim, TiO_2-based photocatalytic disinfection of microbes in aqueous media: a review, Environ. Res. 154 (2017) 296–303, https://doi.org/10.1016/j.envres.2017.01.018.

[16] V. Etacheri, C. Di Valentin, J. Schneider, D. Bahnemann, S.C. Pillai, Visible-light activation of TiO_2 photocatalysts: advances in theory and experiments, J. Photochem. Photobiol. C. 25 (2015) 1–29, https://doi.org/10.1016/j.jphotochemrev.2015.08.003.

[17] D. Chen, Y. Cheng, N. Zhou, P. Chen, Y. Wang, K. Li, S. Huo, P. Cheng, P. Peng, R. Zhang, L. Wang, H. Liu, Y. Liu, R. Ruan, Photocatalytic degradation of organic pollutants using TiO_2-based photocatalysts: a review, J. Clean. Prod. 268 (2020) 121725, https://doi.org/10.1016/j.jclepro.2020.121725.

[18] X. Liu, G. Zhu, X. Wang, X. Yuan, T. Lin, F. Huang, Progress in black titania: a new material for advanced photocatalysis, Adv. Energy Mater. 6 (2016) 1600452, https://doi.org/10.1002/aenm.201600452.

[19] S.G. Ullattil, S.B. Narendranath, S.C. Pillai, P. Periyat, Black TiO_2 nanomaterials: a review of recent advances, Chem. Eng. J. 343 (2018) 708–736, https://doi.org/10.1016/j.cej.2018.01.069.

[20] T.S. Rajaraman, S.P. Parikh, V.G. Gandhi, Black TiO_2: a review of its properties and conflicting trends, Chem. Eng. J. 389 (2020) 123918, https://doi.org/10.1016/j.cej.2019.123918.

[21] W. Fang, M. Xing, J. Zhang, Modifications on reduced titanium dioxide photocatalysts: a review, J. Photochem. Photobiol. C. 32 (2017) 21–39, https://doi.org/10.1016/j.jphotochemrev.2017.05.003.

[22] Z. Li, S. Wang, J. Wu, W. Zhou, Recent progress in defective TiO_2 photocatalysts for energy and environmental applications, Renew. Sust. Energ. Rev. 156 (2022) 111980, https://doi.org/10.1016/j.rser.2021.111980.

[23] M. Xing, W. Fang, M. Nasir, Y. Ma, J. Zhang, M. Anpo, Self-doped Ti^{3+}-enhanced TiO_2 nanoparticles with a high-performance photocatalysis, J. Catal. 297 (2013) 236–243, https://doi.org/10.1016/j.jcat.2012.10.014.

[24] R. Ren, Z. Wen, S. Cui, Y. Hou, X. Guo, J. Chen, Controllable synthesis and tunable photocatalytic properties of Ti^{3+}-doped TiO_2, Sci. Rep. 5 (2015) 10714, https://doi.org/10.1038/srep10714.

[25] H. Tan, Z. Zhao, M. Niu, C. Mao, D. Cao, D. Cheng, P. Feng, Z. Sun, A facile and versatile method for preparation of colored TiO_2 with enhanced solar-driven photocatalytic activity, Nanoscale 6 (2014) 10216–10223, https://doi.org/10.1039/C4NR02677B.

[26] L. Andronic, A. Enesca, Black TiO_2 synthesis by chemical reduction methods for photocatalysis applications, Front. Chem. 8 (2020), https://doi.org/10.3389/fchem.2020.565489.

[27] W. Fang, M. Xing, J. Zhang, A new approach to prepare Ti^{3+} self-doped TiO_2 via $NaBH_4$ reduction and hydrochloric acid treatment, Appl. Catal. B 160–161 (2014) 240–246, https://doi.org/10.1016/j.apcatb.2014.05.031.

[28] S. Liu, S. Yuan, Q. Zhang, B. Xu, C. Wang, M. Zhang, T. Ohno, Fabrication and characterization of black TiO_2 with different Ti^{3+} concentrations under atmospheric conditions, J. Catal. 366 (2018) 282–288, https://doi.org/10.1016/j.jcat.2018.07.018.

[29] N.M. Nursam, X. Wang, R.A. Caruso, High-throughput synthesis and screening of titania-based photocatalysts, ACS Comb. Sci. 17 (2015) 548–569, https://doi.org/10.1021/acscombsci.5b00049.

[30] Y. Bi, P. Westerhoff, High-throughput analysis of photocatalytic reactivity of differing TiO_2 formulations using 96-well microplate reactors, Chemosphere 223 (2019) 275–284, https://doi.org/10.1016/j.chemosphere.2019.02.016.

[31] T.B. Engelhardt, S. Schmitz-Stöwe, T. Schwarz, K. Stöwe, Development of a novel high throughput photo-catalyst screening procedure: UV-A degradation of 17α-ethinylestradiol with doped TiO_2-based photo-catalysts, Materials 13 (2020) 1365, https://doi.org/10.3390/ma13061365.

[32] N. Wang, X. Zhang, Y. Wang, W. Yu, H.L.W. Chan, Microfluidic reactors for photocatalytic water purification, Lab Chip 14 (2014) 1074–1082, https://doi.org/10.1039/C3LC51233A.

[33] M. Yew, Y. Ren, K.S. Koh, C. Sun, C. Snape, A review of state-of-the-art microfluidic technologies for environmental applications: detection and remediation, Glob. Chall. 3 (2019) 1800060, https://doi.org/10.1002/gch2.201800060.

[34] S. Sohrabi, M.K. Moraveji, D. Iranshahi, A review on the design and development of photocatalyst synthesis and application in microfluidic reactors: challenges and opportunities, Rev. Chem. Eng. 36 (2020) 687–722, https://doi.org/10.1515/revce-2018-0013.

[35] K. Shukla, S. Agarwalla, S. Duraiswamy, R.K. Gupta, Recent advances in heterogeneous micro-photoreactors for wastewater treatment application, Chem. Eng. Sci. 235 (2021) 116511, https://doi.org/10.1016/j.ces.2021.116511.

[36] A. Yusuf, C. Garlisi, G. Palmisano, Overview on microfluidic reactors in photocatalysis: Applications of graphene derivatives, Catal. Today 315 (2018) 79–92, https://doi.org/10.1016/j.cattod.2018.05.041.

[37] L. Lei, N. Wang, X.M. Zhang, Q. Tai, D.P. Tsai, H.L.W. Chan, Optofluidic planar reactors for photocatalytic water treatment using solar energy, Biomicrofluidics 4 (2010) 43004, https://doi.org/10.1063/1.3491471.

[38] S. Zhang, J. Zhang, J. Sun, Z. Tang, Capillary microphotoreactor packed with TiO_2-coated glass beads: An efficient tool for photocatalytic reaction, Chem. Eng. Process. 147 (2020) 107746, https://doi.org/10.1016/j.cep.2019.107746.

[39] C. Sambiagio, T. Noël, Flow photochemistry: shine some light on those tubes!, Trends Chem. 2 (2020) 92–106, https://doi.org/10.1016/j.trechm.2019.09.003.

[40] Y. Li, B. Lin, L. Ge, H. Guo, X. Chen, M. Lu, Real-time spectroscopic monitoring of photocatalytic activity promoted by graphene in a microfluidic reactor, Sci. Rep. 6 (2016) 28803, https://doi.org/10.1038/srep28803.

[41] H. Zhang, J.-J. Wang, J. Fan, Q. Fang, Microfluidic chip-based analytical system for rapid screening of photocatalysts, Talanta 116 (2013) 946–950, https://doi.org/10.1016/j.talanta.2013.08.012.

[42] M. Vezzoli, T. Farrell, A. Baker, S. Psaltis, W.N. Martens, J.M. Bell, Optimal catalyst thickness in titanium dioxide fixed film reactors: mathematical modelling and experimental validation, Chem. Eng. J. 234 (2013) 57–65, https://doi.org/10.1016/j.cej.2013.08.049.

[43] V. Chausse, J. Llorca, Photoproduction of hydrogen in microreactors: Catalytic coating or slurry configuration? Catal. Today (2020) https://doi.org/10.1016/j.cattod.2020.08.021.

[44] M.F.J. Dijkstra, A. Michorius, H. Buwalda, H.J. Panneman, J.G.M. Winkelman, A.A. C.M. Beenackers, Comparison of the efficiency of immobilized and suspended systems in photocatalytic degradation, Catal. Today 66 (2001) 487–494, https://doi.org/10.1016/S0920-5861(01)00257-7.

[45] A. Manassero, M.L. Satuf, O.M. Alfano, Photocatalytic reactors with suspended and immobilized TiO_2: comparative efficiency evaluation, Chem. Eng. J. 326 (2017) 29–36, https://doi.org/10.1016/j.cej.2017.05.087.

[46] E. Adamek, W. Baran, J. Ziemiańska-Błaszczyk, A. Sobczak, Immobilisation of TiO_2-P25 on a glass fibre mat: preparation, photocatalytic activity and stability, Sol. Energy 188 (2019) 1232–1242, https://doi.org/10.1016/j.solener.2019.07.034.

[47] R. Zhou, R. Han, M. Bingham, C. O'Rourke, A. Mills, 3D printed, plastic photocatalytic flow reactors for water purification, Photochem. Photobio. Sci. 21 (2022) 1585–1600, https://doi.org/10.1007/s43630-022-00242-y.

[48] R.A. Carcel, L. Andronic, A. Duta, Photocatalytic activity and stability of TiO_2 and WO_3 thin films, Mater. Charact. 70 (2012) 68–73, https://doi.org/10.1016/j.matchar.2012.04.021.

[49] Y. Liu, R. Liu, C. Liu, S. Luo, L. Yang, F. Sui, Y. Teng, R. Yang, Q. Cai, Enhanced photocatalysis on TiO_2 nanotube arrays modified with molecularly imprinted TiO_2 thin film, J. Hazard Mater. 182 (2010) 912–918, https://doi.org/10.1016/j.jhazmat.2010.07.007.

[50] J. Bennani, R. Dillert, T.M. Gesing, D. Bahnemann, Physical properties, stability, and photocatalytic activity of transparent TiO_2/SiO_2 films, Sep Purif. Technol. 67 (2009) 173–179, https://doi.org/10.1016/j.seppur.2009.03.019.

[51] M. Pylnev, M.-S. Wong, Comparative study of photocatalytic deactivation of pure and black titania thin films, J. Photochem. Photobio. A Chem. 378 (2019) 125–130, https://doi.org/10.1016/j.jphotochem.2019.04.020.

[52] M. Zimbone, G. Cacciato, M. Boutinguiza, A. Gulino, M. Cantarella, V. Privitera, M. G. Grimaldi, Hydrogenated black-TiO_x: a facile and scalable synthesis for environmental water purification, Catal. Today 321–322 (2019) 146–157, https://doi.org/10.1016/j.cattod.2018.03.040.

[53] F. Guba, Ü. Tastan, K. Gugeler, M. Buntrock, T. Rommel, D. Ziegenbalg, Rapid prototyping for photochemical reaction engineering, Chem. Ing. Tech. 91 (2019) 17–29, https://doi.org/10.1002/cite.201800035.

[54] J.M. Aguirre-Cortés, A.I. Moral-Rodríguez, E. Bailón-García, A. Davó-Quiñonero, A. F. Pérez-Cadenas, F. Carrasco-Marín, 3D printing in photocatalysis: methods and capabilities for the improved performance, Appl. Mater. Today 32 (2023) 101831, https://doi.org/10.1016/j.apmt.2023.101831.

[55] A.P. Fagundes, J.O. de B. Lira, N. Padoin, C. Soares, H.G. Riella, Additive manufacturing of functional devices for environmental applications: a review, J. Environ. Chem. Eng. 10 (2022) 108049, https://doi.org/10.1016/j.jece.2022.108049.

[56] O.R. Onisuru, O.A. Alimi, K. Potgieter, R. Meijboom, Continuous-flow catalytic degradation of hexacyanoferrate ion through electron transfer induction in a 3D-printed flow reactor, J. Mater. Eng. Perform. 30 (2021) 4891–4901, https://doi.org/10.1007/s11665-021-05527-4.

[57] A. Cabrera, I. Pellejero, T. Oroz-Mateo, C. Salazar, A. Navajas, C. Fernández-Acevedo, L.M. Gandía, Three-dimensional printing of acrylonitrile butadiene styrene microreactors for photocatalytic applications, Ind. Eng. Chem. Res. 59 (2020) 20686–20692, https://doi.org/10.1021/acs.iecr.0c04349.

[58] S.J. Phang, V.-L. Wong, K.H. Cheah, L.-L. Tan, 3D-printed photoreactor with robust g-C_3N_4 homojunction based thermoset coating as a new and sustainable approach for photocatalytic wastewater treatment, J. Environ. Chem. Eng. 9 (2021) 106437, https://doi.org/10.1016/j.jece.2021.106437.

[59] T. Roider, N. Frommknecht, A. Höltzel, U. Tallarek, Device for automated screening of irradiation wavelength and intensity – investigation of the wavelength dependence of photoreactions with an arylazo sulfone in continuous flow, React. Chem. Eng. 7 (2022) 2035–2044, https://doi.org/10.1039/D2RE00142J.

[60] A. Riddell, P. Kvist, D. Bernin, A 3D printed photoreactor for investigating variable reaction geometry, wavelength, and fluid flow, Rev. Sci. Instrum. 93 (2022) 084103, https://doi.org/10.1063/5.0087107.

[61] P.P. Lampkin, B.J. Thompson, S.H. Gellman, Versatile open-source photoreactor architecture for photocatalysis across the visible spectrum, Org. Lett. 23 (2021) 5277–5281, https://doi.org/10.1021/acs.orglett.1c01910.

[62] C. Bogatu, M. Covei, D. Perniu, I. Tismanar, A. Duta, Stability of the Cu_2ZnSnS_4/TiO_2 photocatalytic thin films active under visible light irradiation, Catal. Today 328 (2019) 79–84, https://doi.org/10.1016/j.cattod.2018.11.031.

[63] F. Sgolastra, P. Medrzycki, L. Bortolotti, S. Maini, C. Porrini, N. Simon-Delso, J. Bosch, Bees and pesticide regulation: lessons from the neonicotinoid experience, Biol. Conserv 241 (2020) 108356, https://doi.org/10.1016/j.biocon.2019.108356.

[64] R. Perkins, L. Barron, G. Glauser, M. Whitehead, G. Woodward, D. Goulson, Down-the-drain pathways for fipronil and imidacloprid applied as spot-on parasiticides to dogs: estimating aquatic pollution, Sci. Total Environ. 917 (2024) 170175, https://doi.org/10.1016/j.scitotenv.2024.170175.

[65] M. Egli, H. Rapp-Wright, O. Oloyede, W. Francis, R. Preston-Allen, S. Friedman, G. Woodward, F.B. Piel, L.P. Barron, A One-Health environmental risk assessment of contaminants of emerging concern in London's waterways throughout the SARS-CoV-2 pandemic, Environ. Int 180 (2023) 108210, https://doi.org/10.1016/j.envint.2023.108210.

[66] N.W. Thunnissen, L.S. Lautz, T.W.G. van Schaik, A.J. Hendriks, Ecological risks of imidacloprid to aquatic species in the Netherlands: measured and estimated concentrations compared to species sensitivity distributions, Chemosphere 254 (2020) 126604, https://doi.org/10.1016/j.chemosphere.2020.126604.

[67] D. Chen, F. Li, A.K. Ray, External and internal mass transfer effect on photocatalytic degradation, Catal. Today 66 (2001) 475–485, https://doi.org/10.1016/S0920-5861(01)00256-5.

[68] V.N. Kuznetsov, N. Serpone, On the origin of the spectral bands in the visible absorption spectra of visible-light-active TiO_2 specimens analysis and assignments, J. Phys. Chem. C. 113 (2009) 15110–15123, https://doi.org/10.1021/jp901034t.

[69] P. Makuła, M. Pacia, W. Macyk, How To correctly determine the band gap energy of modified semiconductor photocatalysts based on UV–Vis spectra, J. Phys. Chem. Lett. 9 (2018) 6814–6817, https://doi.org/10.1021/acs.jpclett.8b02892.

[70] R. López, R. Gómez, Band-gap energy estimation from diffuse reflectance measurements on sol–gel and commercial TiO_2: a comparative study, J. Solgel Sci. Technol. 61 (2012) 1–7, https://doi.org/10.1007/s10971-011-2582-9.

[71] E.S. Welter, S. Garg, R. Gläser, M. Goepel, Methodological investigation of the band gap determination of solid semiconductors via UV/Vis spectroscopy, ChemPhotoChem 7 (2023) e202300001, https://doi.org/10.1002/cptc.202300001.

[72] Z. Bielan, S. Dudziak, A. Sulowska, D. Pelczarski, J. Ryl, A. Zielińska-Jurek, Preparation and characterization of defective TiO_2. The effect of the reaction environment on titanium vacancies formation, Materials 13 (2020), https://doi.org/10.3390/ma13122763.

[73] Á. Balog, G.F. Samu, S. Pető, C. Janáky, The mystery of black TiO_2: insights from combined surface science and in situ electrochemical methods, ACS Mater. Au 1 (2021) 157–168, https://doi.org/10.1021/acsmaterialsau.1c00020.

[74] X. Bi, G. Du, A. Kalam, D. Sun, Y. Yu, Q. Su, B. Xu, A.G. Al-Sehemi, Tuning oxygen vacancy content in TiO_2 nanoparticles to enhance the photocatalytic performance, Chem. Eng. Sci. 234 (2021) 116440, https://doi.org/10.1016/j.ces.2021.116440.

[75] J. Klein, L. Kampermann, B. Mockenhaupt, M. Behrens, J. Strunk, G. Bacher, Limitations of the Tauc Plot Method, Adv. Funct. Mater. 33 (2023) 2304523, https://doi.org/10.1002/adfm.202304523.

[76] L. Kampermann, J. Klein, J. Korte, O. Kowollik, O. Pfingsten, T. Smola, S. Saddeler, T.H. Piotrowiak, S. Salamon, J. Landers, H. Wende, A. Ludwig, S. Schulz, G. Bacher, Link between structural and optical properties of $Co_xFe_{3-x}O_4$ nanoparticles and thin films with different Co/Fe ratios, J. Phys. Chem. C. 125 (2021) 14356–14365, https://doi.org/10.1021/acs.jpcc.0c11277.

[77] B.D. Viezbicke, S. Patel, B.E. Davis, D.P. Birnie III, Evaluation of the Tauc method for optical absorption edge determination: ZnO thin films as a model system, Phys. Status Solidi B 252 (2015) 1700–1710, https://doi.org/10.1002/pssb.201552007.

[78] M. He, J. Ji, B. Liu, H. Huang, Reduced TiO_2 with tunable oxygen vacancies for catalytic oxidation of formaldehyde at room temperature, Appl. Surf. Sci. 473 (2019) 934–942, https://doi.org/10.1016/j.apsusc.2018.12.212.

[79] L.A. Ayala-Fonseca, E.J.-C. Amieva, C. Rodriguez-Gonzalez, C. Angeles-Chavez, E. De la Rosa, V.M. Castaño, P. Salas, Enhanced Raman effect of solvothermal synthesized reduced graphene oxide/titanium dioxide nanocomposites, ChemistrySelect 5 (2020) 3789–3797, https://doi.org/10.1002/slct.202000335.

[80] A. Pougin, A. Lüken, C. Klinkhammer, D. Hiltrop, M. Kauer, K. Tölle, M. Havenith-Newen, K. Morgenstern, W. Grünert, M. Muhler, J. Strunk, Probing oxide reduction and phase transformations at the Au-TiO_2 interface by vibrational spectroscopy, Top. Catal. 60 (2017) 1744–1753, https://doi.org/10.1007/s11244-017-0851-8.

[81] T. Hanawa, A comprehensive review of techniques for biofunctionalization of titanium, Jpis 41 (2011) 263–272, https://doi.org/10.5051/jpis.2011.41.6.263.

[82] D. Ariyanti, L. Mills, J. Dong, Y. Yao, W. Gao, $NaBH_4$ modified TiO_2: defect site enhancement related to its photocatalytic activity, Mater. Chem. Phys. 199 (2017) 571–576, https://doi.org/10.1016/j.matchemphys.2017.07.054.

[83] J. Yan, G. Wu, N. Guan, L. Li, Z. Li, X. Cao, Understanding the effect of surface/bulk defects on the photocatalytic activity of TiO_2: anatase versus rutile, Phys. Chem. Chem. Phys. 15 (2013) 10978–10988, https://doi.org/10.1039/C3CP50927C.

[84] M. Kong, Y. Li, X. Chen, T. Tian, P. Fang, F. Zheng, X. Zhao, Tuning the relative concentration ratio of bulk defects to surface defects in TiO_2 nanocrystals leads to high photocatalytic efficiency, J. Am. Chem. Soc. 133 (2011) 16414–16417, https://doi.org/10.1021/ja207826q.

[85] M. Janczarek, E. Kowalska, Defective dopant-free TiO_2 as an efficient visible light-active photocatalyst, Catalysts 11 (2021), https://doi.org/10.3390/catal11080978.

[86] S.A. Sabinas-Hernández, J.M. Gracia Jiménez, N.R. Silva González, M.P. Elizalde-González, U. Salazar-Kuri, S. Tehuacanero-Cuapa, Blue titania: the outcome of defects, crystalline-disordered core-shell structure, and hydrophilicity change, Nanomaterials 12 (2022), https://doi.org/10.3390/nano12091501.

[87] L. Andronic, M. Lelis, A. Enesca, S. Karazhanov, Photocatalytic activity of defective black-titanium oxide photocatalysts towards pesticide degradation under UV/VIS irradiation, Surf. Interfaces 32 (2022) 102123, https://doi.org/10.1016/j.surfin.2022.102123.

[88] M.L. Satuf, J. Macagno, A. Manassero, G. Bernal, P.A. Kler, C.L.A. Berli, Simple method for the assessment of intrinsic kinetic constants in photocatalytic microreactors, Appl. Catal. B. 241 (2019) 8–17, https://doi.org/10.1016/j.apcatb.2018.09.015.

[89] B. Liu, B. Zhang, G. Dong, F. Wu, B. Chen, A UVA light-emitting diode microreactor for the photocatalytic degradation of humic acids and the control of disinfection by-products formation potential, J. Clean. Prod. 429 (2023) 139395, https://doi.org/10.1016/j.jclepro.2023.139395.

[90] X. Zhan, C. Yan, Y. Zhang, G. Rinke, G. Rabsch, M. Klumpp, A.I. Schäfer, R. Dittmeyer, Investigation of the reaction kinetics of photocatalytic pollutant degradation under defined conditions with inkjet-printed TiO_2 films – from batch to a novel continuous-flow microreactor, React. Chem. Eng. 5 (2020) 1658–1670, https://doi.org/10.1039/D0RE00238K.